Progress In Electromagnetics Research, Vol. 168, 15–23, 2020

Superscattering of Light in Refractive-Index Near-Zero Environments

Chan Wang[1, 2], Chao Qian[1], Hao Hu[3], Lian Shen[1], Zuojia Wang[4], Huaping Wang[2, *], Zhiwei Xu[2], Baile Zhang[5, 6], Hongsheng Chen[1], and Xiao Lin[1, 6, *]

Abstract—Enhancing the scattering of light from subwavelength structures is of both fundamental and practical significance. While the scattering cross section from each channel cannot exceed the single-channel limit, it is recently reported that the total cross section can far exceed this limit if one overlaps the contribution from many channels. Such a phenomenon about enhancing the scattering from subwavelength structures in *free space* is denoted as the superscattering in some literature. However, the scatterer in practical scenarios is not always in *free space* but may be embedded in environments with non-unity refractive index n. The influence of environments on the superscattering remains elusive. Here the superscattering from subwavelength structures in the isotropic environment with near-zero index are theoretically investigated. Importantly, a smaller n can lead to a larger total cross section for superscattering. The underlying mechanism is that a smaller n can give rise to a larger single-channel limit. Our work thus indicates that the scattering from subwavelength structures can be further enhanced if one simultaneously maximizes the single-channel limit and the contribution from many channels.

1. INTRODUCTION

The electromagnetic scattering, as a ubiquitous physical process in our daily life, has wide practical applications in various fields [1–15], such as telecommunications, photonics, biophysics, nanotechnology, material science, and military facilities. The *absolute* scattering cross section [16–19], which is the ratio of the total scattered power over the intensity of incident waves, is a key parameter to quantitatively characterize the electromagnetic scattering. As such, it is of fundamental importance to flexibly control the scattering cross section [5, 20–27], particularly to enhance the scattering cross section for tiny (e.g., subwavelength) object [6, 22, 26, 28–30]. However, the maximum theoretical value of scattering cross section from each channel in *free space* can only reach $2\lambda_0/\pi$ in two dimensions (2D) or $(2m+1)\lambda_0^2/2\pi$ (m is an integer) in three dimensions (3D) [16, 17, 31–34], where λ_0 is the wavelength of light in *free space*. Such a scattering limit is denoted as the single-channel limit in some literature [16, 17]. To overcome the single-channel limit, the phenomenon of superscattering from subwavelength structures in *free space* was theoretically proposed in 2010 [16] and was observed in experiment in 2019 [34]. The superscattering can allow the subwavelength structures to achieve their total cross section far exceeding the single-channel limit. The underlying mechanism of superscattering is the degenerate resonance or to overlap the scattering contribution of many channels at the same frequency. As such, the superscattering

Received 4 July 2020, Accepted 12 August 2020, Scheduled 22 August 2020

* Corresponding author: Xiao Lin (xiaolinbnwj@gmail.com), Huaping Wang (hpwang@zju.edu.cn).

[1] Key Laboratory of Advanced Micro/Nano Electronic Devices & Smart Systems of Zhejiang, The Electromagnetics Academy at Zhejiang University, Zhejiang University, Hangzhou 310027, China. [2] Key Laboratory of Ocean Observation-Imaging Testbed of Zhejiang Province, The Institute of Marine Electronics Engineering, Ocean College, Zhejiang University, Zhoushan 316021, China. [3] School of Electrical and Electronic Engineering, Nanyang Technological University, Nanyang Avenue, Singapore 639798, Singapore. [4] School of Information Science and Engineering, Shandong University, Qingdao 266237, China. [5] Centre for Disruptive Photonic Technologies, NTU, Singapore 637371, Singapore. [6] Division of Physics and Applied Physics, School of Physical and Mathematical Sciences, Nanyang Technological University, Singapore 637371, Singapore.

provides us an exotic way to enhance the light-matter interaction at the subwavelength scale in *free space*, and it would have wide practical applications ranging from sensing, optical imaging, optical tagging to spectroscopy.

On the other hand, it is necessary to note that not all scatterers are in *free space*. There are many scattering phenomena (e.g., fluorescence imaging) [35] existing in complex environments. Correspondingly, the designed scatterers may be embedded in homogeneous environments with non-unity refractive index $n \neq 1$ (e.g., liquids) and even in inhomogeneous environments (e.g., waveguides, photonic crystals, and biological tissues) [35–43], depending on the application scenarios. It is then important to explore the possibility of realizing the superscattering in various environments. Moreover, it would be fundamental to explore the influence of environments on the superscattering. In spite of fundamental interest, these issues remain unexplored yet.

In this work, we theoretically investigate the superscattering from subwavelength structures in transparent and isotropic environments with $n < 1$, especially for those with $n \to 0$. Importantly, we find that the superscattering in lower-index environments can enable a much larger total cross section for subwavelength structures. We note that in environments with near-zero index, although the superscattering was not achieved before, the extraordinarily large cross section for individual nano-resonators is known to be theoretically achievable as reported in 2015 [33]. The underlying mechanism for the extraordinarily large superscattering in low-index environments, in accordance with Ref. [33], is that the environment with a lower value of n can give rise to a much larger single-channel limit. Our work suggests that the combined optimization strategy of the single-channel limit and the contribution from many channels could provide a powerful way to largely enhance the scattering from tiny objects. As such, our proposed design strategy can provide useful guidance to strengthen light-matter interactions at the subwavelength scale, and it can benefit a wealth of applications requiring large scattering, such as the design of nano-antennas, energy harvesting, and nano-photonics.

2. MAIN RESULTS

We begin by briefly revisiting the scattering in environments with low or near-zero index. In experiments, the transparent or low-loss environments with low or near-zero index can be effectively constructed, for example, by waveguides [36, 37, 43], doped epsilon-near-zero materials [44, 45], photonic crystals with Dirac cones [35], and metamaterials [46–49]. For conceptual clarity, we consider the superscattering from a 2D subwavelength rod in the transparent environment [inset in Figure 1]. Meanwhile, we consider the incidence of transverse-magnetic (TM, or p-polarized) plane waves. According to the electromagnetic wave theory, the total magnetic field in the surrounding environment in the cylindrical coordinates can be written as

$$\overline{H}_{z,\,\mathrm{total}} = \hat{z} H_0 \sum\nolimits_{m=-\infty}^{\infty} \left(i^m J_m(k\rho) e^{im\phi} + i^m S_m H_m^{(1)}(k\rho) e^{im\phi} \right) \tag{1}$$

In above, $H_m^{(1)}$ and J_m are the mth order of Hankel function and Bessel function of the first kind, respectively. $k = n\omega/c = \sqrt{\varepsilon_r \mu_r} \cdot \omega/c$ is the wave vector of light in the surrounding environment, and we simply let $\varepsilon_r = \mu_r > 0$ in the analysis, where ε_r and μ_r are the relative permittivity and permeability of environment, respectively; ω is the angular frequency; and c is the speed of light in *free space*. The unknown parameter S_m, namely the scattering coefficient of the mth angular momentum channel, can be analytically solved by matching the boundary conditions [27, 34].

If we let the magnitude of the incident magnetic field to be $H_0 = \sqrt{\frac{\mathrm{Watt}}{\mathrm{meter}} \frac{\omega \varepsilon_0 \varepsilon_r}{2}}$ [16, 27, 34], the corresponding total scattering cross section C_{SCS} can be derived as follows

$$C_{\mathrm{SCS}} = \sum\nolimits_{m=-\infty}^{\infty} C_{\mathrm{SCS},\,m} \tag{2}$$

$$C_{\mathrm{SCS},\,m} = \frac{2\lambda_0}{n\pi} |S_m|^2 = \frac{2\lambda_0}{n\pi} \left| \frac{R_m - 1}{2} \right|^2 \tag{3}$$

where $\lambda_0 = 2\pi c/\omega$ is the wavelength in *free space*. In Equation (3), $C_{\mathrm{SCS},\,m}$ represents the scattering cross section from the individual mth channel; the reflection coefficient R_m in the cylindrical coordinates is defined as $R_m = 1 + 2S_m$ [16, 27, 34]. Due to the energy conservation in passive systems, the reflection

coefficient is subject to $|R_m| \leq 1$. Then it is straightforward to obtain the upper limit for all possible values of $C_{\mathrm{SCS},m}$ in Equation (3). That is,

$$C_{\mathrm{SCS},m} \leq 1/n \cdot 2\lambda_0/\pi \tag{4}$$

Accordingly, for arbitrary value of n, $1/n{\cdot}2\lambda_0/\pi$ is denoted as the single-channel limit for the scattering in the environment with refractive index n in 2D [33]. Similarly, one may derive the single-channel limit of $1/n^2 \cdot (2m+1)\lambda_0^2/2\pi$ for the scattering in the environment with refractive index n in 3D [33]. According to Equation (3), $C_{\mathrm{SCS},m}$ can reach the single-channel limit if $R_m = -1$. Importantly, Equation (4) indicates that a smaller value of n can give rise to a larger single-channel limit. In particular, if $n \to 0$, the single-channel limit can go to infinity. Such an extremely-large single-channel limit enables the extraordinarily large cross section for single nano-resonators in low-index environments as theoretically reported in [33], even without the appearance of superscattering.

Figure 1 shows the theoretical upper limit for the total cross section of subwavelength structures as a function of the refractive index n of environment. In order to emphasize the contribution of scattering from the resonance (i.e., $m \geq 1$), we define the total cross section without considering the contribution from channel $m = 0$ in Figure 1. Figure 1(a) shows that a smaller n or a larger allowed $\max(|m|)$ gives rise to a larger upper limit for the total cross section. To be specific, the upper limit of the total cross section becomes $2 \cdot \max(|m|)/n \cdot 2\lambda_0/\pi$. In other words, a larger single-channel limit and the maximization of the contribution from more channels enable a larger upper limit for the total cross section.

As such, it is reasonable to expect that the superscattering in low-index environments [$n = 0.5$ in Figure 1(c)] would have a much larger total cross section than that of the superscattering in *free space* [$n = 1$ in Figure 1(b)] and that of the non-superscattering in low-index environments [$n = 0.5$ in Figure 1(d)]. For these three scattering scenarios, we show the flow of Poynting vectors of the total fields in Figures 1(b)–(d). Correspondingly, the disturbance of subwavelength scatterer to the power flow of incident waves is the largest in Figure 1(c) among all scenarios. Figure 1 thus implies

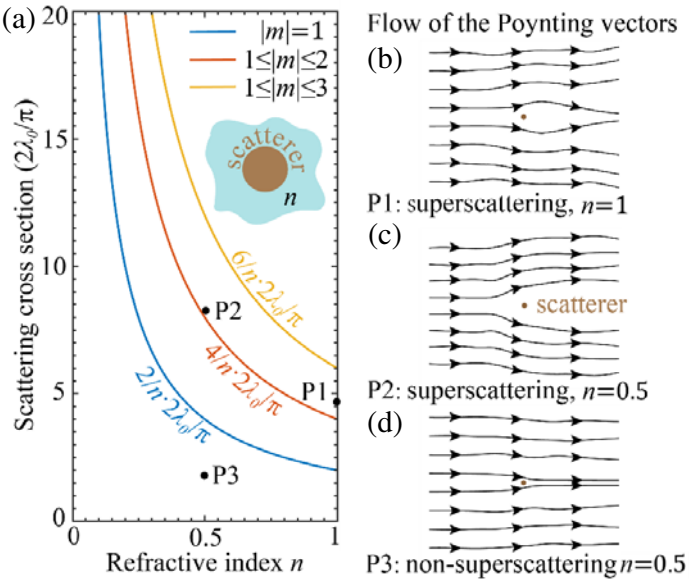

Figure 1. Schematic of superscattering from subwavelength structures in low-index environments. The 2D scatterer is located in the environment with a refractive index n. (a) Upper limit of the total cross section for different numbers of channels. The scattering contribution from the channel $m = 0$ is artificially neglected for all solid lines but is considered in cases (P1–P3). (b)–(d) Flow of the Poynting vectors of total fields outside the scatterer. Here the incident TM waves propagate from left to right. The structural setups of the scatterer in (b) and (c) are the same as that in Figures 3(a) and (b), respectively. In (d), we replace the scatterer in (c) with a dielectric rod of the same diameter with a relative permittivity of $\varepsilon_d = 1.44$. $\lambda_0 = 2\pi c/\omega$ is the operating wavelength in *free space*.

that the superscattering in low-index environments can provide a powerful way to achieve extremely large scattering for subwavelength structures. We highlight that the combined design strategy to simultaneously enlarge the single-channel limit and the contribution from many channels has never been demonstrated before.

3. OPTIMIZATION AND SIMULATION

We now proceed to discuss the possible realization of superscattering from subwavelength structures in low-index environments. As conceptual demonstration, below we consider two different scenarios of superscattering from multilayered and subwavelength rods in environments with $n \leq 1$ in Figures 2–4. To be specific, one is based on the degenerate resonance of phonon polaritons in a thin slab of hexagonal boron nitride (BN) [Figures 2–3], and the other is based on the degenerate resonance of metal plasmons in the metal-dielectric-metal structure [Figure 4]. It is worthy to note that the first theoretical demonstration of superscattering in *free space* is just based on the metal-dielectric-metal structure [16], and the phenomenon of multifrequency superscattering in *free space* is proposed based on the thin BN slab [27]. Here the experimental data of permittivity for BN [10, 50, 51] and metals (e.g., copper) [52] are adopted in the calculation. For conceptual clarity, the imaginary parts of their permittivities are artificially neglected in Figures 2–4. As complementary information, the superscattering based on the realistic lossy BN and metals are shown in Figures S1 and S2 in the supporting information, respectively. In short, the phenomenon of superscattering would survive for scenarios with reasonable amount of loss.

3.1. Superscattering from BN-Based Rod in Different Environments

Figure 2 shows the superscattering of TM waves from the subwavelength and a two-layered rod based on BN in environments with $n \leq 1$. As schematically shown in the inset of Figure 2(a), the two-layered rod is constructed by the innermost dielectric region, which has a relative permittivity of ε_d, a radius of ρ_1, and the outmost shell of BN with a thickness of $\rho_2 - \rho_1$. As comparison, we consider the environment with three different refractive indices, namely $n_1 = 1$ in Figure 2(a), $n_2 = 0.5$ in Figure 2(b), and $n_3 = 0.3$ in Figure 2(c). The superscattering in lower-index environment (e.g., $n = 0.1$) can be

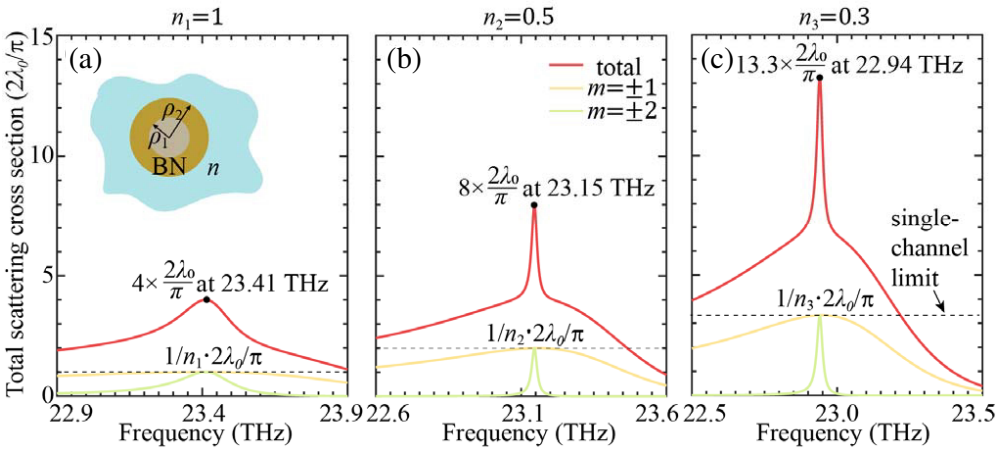

Figure 2. Superscattering in low-index environments induced by the degenerate resonance of BN's phonon polaritons. (a)–(c) Total cross sections of the subwavelength scatterers in the environment with (a) $n_1 = 1$, (b) $n_2 = 0.5$ and (c) $n_3 = 0.3$. Here the scattering cross section from channels with $|m| > 2$ are negligible and the scattering cross section from the channel $m = 0$ is artificially neglected. The basic structural setup is shown in the inset of (a). ρ_1 and $\rho_2 - \rho_1$ are the radius of the innermost dielectric region and the thickness of BN shell, respectively. After the structural optimization, we have $\rho_1 = 1.78\,\mu$m, $\rho_2 = 2.65\,\mu$m and $\varepsilon_d = 5$ in (a), $\rho_1 = 1.69\,\mu$m, $\rho_2 = 3.29\,\mu$m and $\varepsilon_d = 1.44$ in (b), $\rho_1 = 1.8\,\mu$m, $\rho_2 = 5.88\,\mu$m and $\varepsilon_d = 1.14$ in (c), where ε_d is the relative permittivity of the innermost dielectric region.

found in Figures S3 and S4 in the supporting information. To achieve the superscattering in various environments, the related geometrical and material parameters, such as ρ_1, ρ_2, and ε_d in Figure 2, are chosen as the free parameters during the structural optimization. To be specific, the designed subwavelength structures are optimized by the simulated annealing algorithm and by following our previous works of superscattering [27, 34]. In Figure 2, the structural optimization mainly maximizes the scattering contribution from channels with $m = \pm 1$ and $m = \pm 2$ at a frequency within the first reststrahlen band of BN.

After the structural optimization, we show in Figure 2 the total cross section for the superscattering in different environments. Figures 2(a)–(c) show that if the environment has a lower value of n, the FWHM (full width at half maximum) of the peak for the total cross section would become narrower. This indicates that the superscattering phenomenon in lower-index environments is more sensitive to the working frequency. Regarding the frequency, we are mainly interested in the narrow frequency range having the superscattering phenomenon. Within such a narrow working bandwidth, the frequency dispersion for environments is generally negligible. Moreover, the peak value of total cross section reaches $4/n_1 \cdot 2\lambda_0/\pi = 4 \times 2\lambda_0/\pi$ at 23.41 THz in Figure 2(a), $4/n_2 \cdot 2\lambda_0/\pi = 8 \times 2\lambda_0/\pi$ at 23.15 THz in Figure 2(b), and $4/n_3 \cdot 2\lambda_0/\pi = 13.3 \times 2\lambda_0/\pi$ at 22.94 THz in Figure 2(c). The results in Figure 2 then numerically prove that the superscattering at a lower-index environment can give rise to a larger total cross section. More discussion about the influence of environment's refractive index variation on the superscattering phenomenon is given in Figure S5. In addition, we also show in Figure S5 in the supporting information the superscattering phenomenon in low-index environments with $\varepsilon_r \neq \mu_r$.

Figure 3 provides another way to understand the influence of environments on the superscattering in Figure 2, by correspondingly showing the field distribution [Figures 3(a)–(c)] and the scattering cross section per azimuthal angle [Figures 3(d)–(f)]. Figures 3(a)–(c) show that the incident plane waves are severely disturbed in the forward direction. As such, a clear "shadow" emerges behind the scatterer.

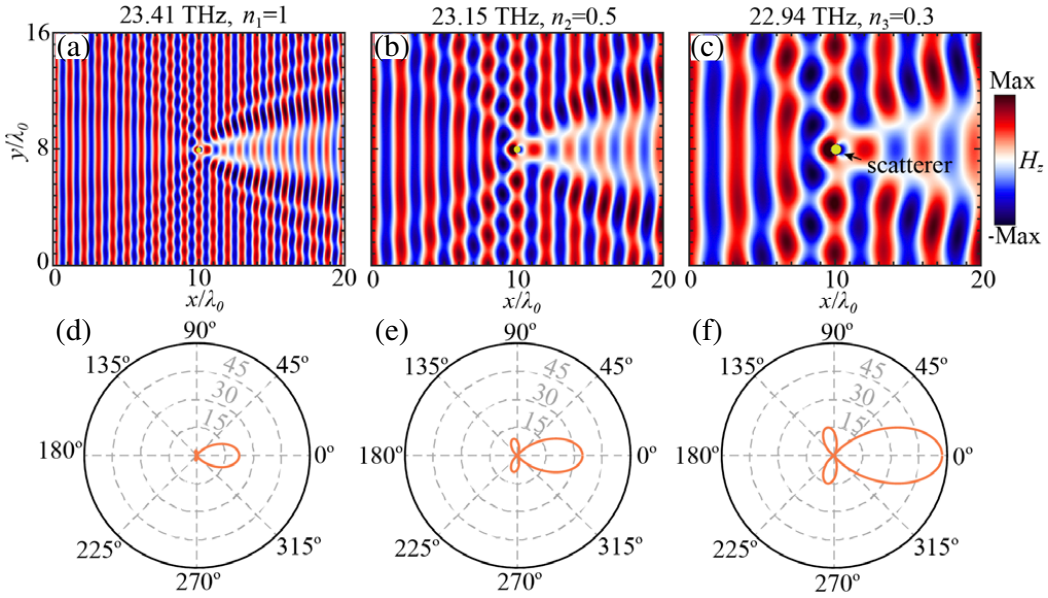

Figure 3. Near-field and far-field demonstration of superscattering in low-index environments. (a)–(c) Distributions of magnetic field H_z around the scatterer and (d)–(f) scattering cross sections per azimuthal angle in the far field at (a), (d) 23.41 THz, (b), (e) 23.15 THz and (c), (f) 22.94 THz. These three frequencies correspond to the peak frequencies of the total cross section in Figures 2(a)–(c), respectively. $\lambda_0 = 2\pi c/\omega$ in (a)–(c) is the operating wavelength in *free space*, where the value of frequency is indicated in each panel. The structural setups in (a), (d), (b), (e) and (c), (f) are the same as those in Figure 2(a), Figure 2(b) and Figure 2(c), respectively. The incident TM waves propagate from left to right in (a)–(c). The radial length in (d)–(f) represents the magnitude of cross section per azimuthal angle and is in unit of $2\lambda_0/\pi$. The flow of the Poynting vectors in (a) and (b) are schematically shown in Figure 1(b) and Figure 1(d), respectively.

Moreover, the "shadow" would become more significant if the environment has a lower value of n. Figures 3(d)–(f) show that the scattered waves appear mostly in the forward direction, in accordance with Figures 3(a)–(c). The underlying reason for these scattering phenomena, as given in our previous works about superscattering [27, 34], is that the scattering fields from channel $|m| = 1$ are in-phase in the forward direction but out-of-phase in the backward direction with the scattered fields from channel $|m| = 2$ [27]. Such a phase difference between scattered fields from different channels then leads to the constructive (destructive) interference in the forward (backward) direction.

3.2. Superscattering from BN-Based Rod in Different Environments

We discuss in Figure 4 the possibility to use another subwavelength metal-based structure to realize the superscattering of TM waves in environments with $n \leq 1$. To be specific, the subwavelength rod is constructed by a three-layered (i.e., metal-dielectric-metal) structure; see the inset of Figure 4(a). After structural optimization, the metal-based subwavelength rod can also achieve the superscattering in various environments, such as $n_1 = 1$ in Figure 4(a), $n_2 = 0.5$ in Figure 4(b), and $n_3 = 0.3$ in Figure 4(c). Correspondingly, the related field distribution and the scattering cross section per azimuthal angle for the superscattering in Figure 4 are shown in Figure S6 in the supporting information. The main results in Figure 4 are in accordance with those in Figure 2. Both Figures 2 and 4 indicate that the degenerate polaritonic resonance can facilitate the realization of superscattering in various environments.

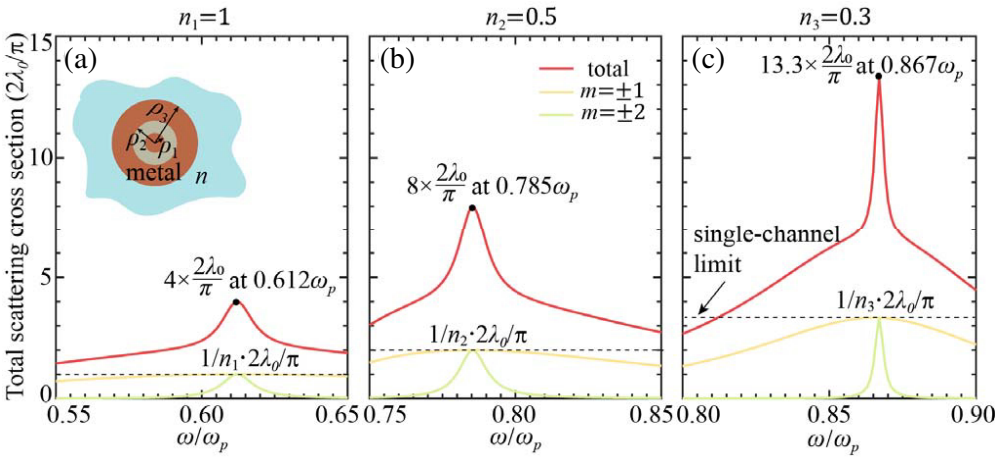

Figure 4. Superscattering in low-index environments induced by the degenerate resonance of metal plasmons. (a)–(c) Total cross sections of the subwavelength scatterers in the environment with (a) $n_1 = 1$, (b) $n_2 = 0.5$ and (c) $n_3 = 0.3$. The basic structural setup is shown in the inset of (a). ρ_1, $\rho_2 - \rho_1$ and $\rho_3 - \rho_2$ are the radius of innermost metal, the thickness of dielectric, and the thickness of outmost metal, respectively. After the structural optimization, we have $\rho_1 = 0.095\lambda_p$, $\rho_2 = 0.131\lambda_p$, $\rho_3 = 0.203\lambda_p$ and $\varepsilon_d = 2.7$ in (b), $\rho_1 = 0.026\lambda_p$ nm, $\rho_2 = 0.057\lambda_p$, $\rho_3 = 0.276\lambda_p$ and $\varepsilon_d = 2.4$ in (b), $\rho_1 = 0.036\lambda_p$, $\rho_2 = 0.142\lambda_p$, $\rho_3 = 0.328\lambda_p$ and $\varepsilon_d = 2.7$ in (c), where ε_d is the relative permittivity of dielectric, $\lambda_p = 2\pi c/\omega_p$, and ω_p is the plasma frequency of metals (e.g., copper).

During the structural optimization, one may also choose to maximize the scattering contribution from more channels so that one can obtain a larger total cross section for tiny object. For example, as a complementary information for Figures 2 and 4, Figures S7 and S8 in the supporting information show the superscattering in environments with $n < 1$ by maximizing the contribution from channels with $m = \pm1$, $m = \pm2$, and $m = \pm3$. Moreover, in addition to the 2D superscattering, it is also possible to realize the 3D superscattering in low-index environments, as shown in Figure S9 in the supporting information. Finally, the superscattering in a realistic low-index environment is also studied in Figure S10 in the supporting information, where we use a metal-based parallel-plate waveguide to model the low-index environment at the microwave regime. Due to the feasibility and convenience to construct the parallel-plate waveguide, the results in Figure S10 in the supporting information may stimulate further experimental verification.

4. CONCLUSION

In conclusion, we theoretically realize the superscattering in environments with non-unity refractive index and systematically discuss the influence of environments on the superscattering. We reveal that since the environment with a lower refractive index can enable a larger single-channel limit, it can give rise to a larger total cross section for the superscattering phenomenon. As such, the simultaneous maximization of the single-channel limit and the contribution from many channels can be a combined strategy to flexibly tailor the scattering from tiny object. Such a combined design strategy for the extremely large electromagnetic scattering should be valuable to various practical applications, such as energy-harvesting, sensing, imaging, etc.

SUPPORTING INFORMATION

This part provides the discussion of the influence of loss on the superscattering, more examples of superscattering in low-index environments, more information for the superscattering in Figure 4, and superscattering in low-index environments by maximizing the contribution from more channels. The supporting figures can be found at the end of the paper.

ACKNOWLEDGMENT

C. Wang and C. Qian contributed equally to this work. This work at Zhejiang University was sponsored by the National Natural Science Foundation of China (NNSFC) under Grants No. 61625502, No. 11961141010, No. 61975176, No. 61775193, and No. 11704332. B. Z. was sponsored by the Singapore Ministry of Education (Grant No. MOE2018-T2-1-022 (S), MOE2016-T3-1-006).

CONFLICT OF INTEREST

The authors declare no conflict of interest.

REFERENCES

1. Aizpurua, J., P. Hanarp, D. S. Sutherland, M. Käll, G. W. Bryant, and F. J. García de Abajo, "Optical properties of gold nanorings," *Phys. Rev. Lett.*, Vol. 90, 057401, 2003.
2. Tribelsky, M. I. and B. S. Luk'Yanchuk, "Anomalous light scattering by small particles," *Phys. Rev. Lett.*, Vol. 97, 263902, 2006.
3. Tang, L., S. E. Kocabas, S. Latif, A. K. Okyay, D.-S. Ly-Gagnon, K. C. Saraswat, and D. A. Miller, "Nanometre-scale germanium photodetector enhanced by a near-infrared dipole antenna," *Nat. Photon.*, Vol. 2, 226–229, 2008.
4. Alu, A. and N. Engheta, "Cloaking a sensor," *Phys. Rev. Lett.*, Vol. 102, 233901, 2009.
5. Atwater, H. A. and A. Polman, "Plasmonics for improved photovoltaic devices," *Nat. Mater.*, Vol. 9, 205–213, 2010.
6. Liu, N., M. L. Tang, M. Hentschel, H. Giessen, and A. P. Alivisatos, "Nanoantenna-enhanced gas sensing in a single tailored nanofocus," *Nat. Mater.*, Vol. 10, 631–636, 2011.
7. Yao, J., X. Yang, X. Yin, G. Bartal, and X. Zhang, "Three-dimensional nanometer-scale optical cavities of indefinite medium," *PNAS*, Vol. 108, 11327–11331, 2011.
8. Chen, P.-Y. and A. Alu, "Atomically thin surface cloak using graphene monolayers," *ACS Nano*, Vol. 5, 5855–5863, 2011.
9. Staude, I., A. E. Miroshnichenko, M. Decker, N. T. Fofang, S. Liu, E. Gonzales, J. Dominguez, T. S. Luk, D. N. Neshev, and I. Brener, "Tailoring directional scattering through magnetic and electric resonances in subwavelength silicon nanodisks," *ACS Nano*, Vol. 7, 7824–7832, 2013.
10. Lin, X., Y. Yang, N. Rivera, J. J. López, Y. Shen, I. Kaminer, H. Chen, B. Zhang, J. D. Joannopoulos, and M. Soljačić, "All-angle negative refraction of highly squeezed plasmon and phonon polaritons in graphene-boron nitride heterostructures," *PNAS*, Vol. 114, 6717–6721, 2017.

11. Lin, X., S. Easo, Y. Shen, H. Chen, B. Zhang, J. D. Joannopoulos, M. Soljačić, and I. Kaminer, "Controlling Cherenkov angles with resonance transition radiation," *Nat. Phys.*, Vol. 14, 816–821, 2018.
12. Shi, X., X. Lin, I. Kaminer, F. Gao, Z. Yang, J. D. Joannopoulos, M. Soljačić, and B. Zhang, "Superlight inverse Doppler effect," *Nat. Phys.*, Vol. 14, 1001–1005, 2018.
13. Shen, L., X. Lin, M. Y. Shalaginov, T. Low, X. Zhang, B. Zhang, and H. Chen, "Broadband enhancement of on-chip single-photon extraction via tilted hyperbolic metamaterials," *Appl. Phys. Rev.*, Vol. 7, 021403, 2020.
14. Qian, C., X. Lin, X. Lin, J. Xu, Y. Sun, E. Li, B. Zhang, and H. Chen, "Performing optical logic operations by a diffractive neural network," *Light Sci. Appl.*, Vol. 9, 59, 2020.
15. Hu, H., X. Lin, J. Zhang, D. Liu, P. Genevet, B. Zhang, and Y. Luo, "Nonlocality induced Cherenkov threshold," *Laser Photonics Rev.*, 2000149, 2020.
16. Ruan, Z. and S. Fan, "Superscattering of light from subwavelength nanostructures," *Phys. Rev. Lett.*, Vol. 105, 013901, 2010.
17. Ruan, Z. and S. Fan, "Design of subwavelength superscattering nanospheres," *Appl. Phys. Lett.*, Vol. 98, 043101, 2011.
18. Miller, O. D., C. W. Hsu, M. H. Reid, W. Qiu, B. G. De Lacy, J. D. Joannopoulos, M. Soljačić, and S. G. Johnson, "Fundamental limits to extinction by metallic nanoparticles," *Phys. Rev. Lett.*, Vol. 112, 123903, 2014.
19. Yang, Y., O. D. Miller, T. Christensen, J. D. Joannopoulos, and M. Soljacic, "Low-loss plasmonic dielectric nanoresonators," *Nano Lett.*, Vol. 17, 3238–3245, 2017.
20. Yu, Z., G. Veronis, S. Fan, and M. L. Brongersma, "Design of midinfrared photodetectors enhanced by surface plasmons on grating structures," *Appl. Phys. Lett.*, Vol. 89, 151116, 2006.
21. Hao, J., W. Yan, and M. Qiu, "Super-reflection and cloaking based on zero index metamaterial," *Appl. Phys. Lett.*, Vol. 96, 101109, 2010.
22. Mirzaei, A., I. V. Shadrivov, A. E. Miroshnichenko, and Y. S. Kivshar, "Cloaking and enhanced scattering of core-shell plasmonic nanowires," *Opt. Express*, Vol. 21, 10454–10459, 2013.
23. Coenen, T., F. B. Arango, A. F. Koenderink, and A. Polman, "Directional emission from a single plasmonic scatterer," *Nat. Commun.*, Vol. 5, 3250, 2014.
24. Yu, N. and F. Capasso, "Flat optics with designer metasurfaces," *Nat. Mater.*, Vol. 13, 139–150, 2014.
25. Poddubny, A., I. Iorsh, P. Belov, and Y. Kivshar, "Hyperbolic metamaterials," *Nat. Photon.*, Vol. 7, 948–957, 2013.
26. Li, R., B. Zheng, X. Lin, R. Hao, S. Lin, W. Yin, E. Li, and H. Chen, "Design of ultracompact graphene-based superscatterers," *IEEE J. Sel. Top. Quant.*, Vol. 23, 4600208, 2017.
27. Qian, C., X. Lin, Y. Yang, F. Gao, Y. Shen, J. Lopez, I. Kaminer, B. Zhang, E. Li, M. Soljačić, and H. Chen, "Multifrequency superscattering from subwavelength hyperbolic structures," *ACS Photon.*, Vol. 5, 1506–1511, 2018.
28. Bohren, C. F. and D. R. Huffman, *Absorption and Scattering of Light by Small Particles*, John Wiley & Sons, New Jersey, 1998.
29. Brolo, A. G., E. Arctander, R. Gordon, B. Leathem, and K. L. Kavanagh, "Nanohole-enhanced Raman scattering," *Nano Lett.*, Vol. 4, 2015–2018, 2004.
30. Rakich, P. T., C. Reinke, R. Camacho, P. Davids, and Z. Wang, "Giant enhancement of stimulated Brillouin scattering in the subwavelength limit," *Phys. Rev. X*, Vol. 2, 011008, 2012.
31. Foot, C. J., *Atomic Physics*, Oxford University Press, New York, 2005.
32. Verslegers, L., Z. Yu, Z. Ruan, P. B. Catrysse, and S. Fan, "From electromagnetically induced transparency to superscattering with a single structure: A coupled-mode theory for doubly resonant structures," *Phys. Rev. Lett.*, Vol. 108, 083902, 2012.
33. Zhou, M., L. Shi, J. Zi, and Z. Yu, "Extraordinarily large optical cross section for localized single nanoresonator," *Phys. Rev. Lett.*, Vol. 115, 023903, 2015.

34. Qian, C., X. Lin, Y. Yang, X. Xiong, H. Wang, E. Li, I. Kaminer, B. Zhang, and H. Chen, "Experimental observation of superscattering," *Phys. Rev. Lett.*, Vol. 122, 063901, 2019.
35. Kinkhabwala, A., Z. Yu, S. Fan, Y. Avlasevich, K. Müllen, and W. E. Moerner, "Large single-molecule fluorescence enhancements produced by a bowtie nanoantenna," *Nat. Photon.*, Vol. 3, 654–657, 2009.
36. Silveirinha, M. and N. Engheta, "Tunneling of electromagnetic energy through subwavelength channels and bends using ε-near-zero materials," *Phys. Rev. Lett.*, Vol. 97, 157403, 2006.
37. Edwards, B., A. Alu, M. E. Young, M. Silveirinha, and N. Engheta, "Experimental verification of epsilon-near-zero metamaterial coupling and energy squeezing using a microwave waveguide," *Phys. Rev. Lett.*, Vol. 100, 033903, 2008.
38. Huang, X., Y. Lai, Z. H. Hang, H. Zheng, and C. T. Chan, "Dirac cones induced by accidental degeneracy in photonic crystals and zero-refractive-index materials," *Nat. Mater.*, Vol. 10, 582–586, 2011.
39. Kocaman, S., M. Aras, P. Hsieh, J. McMillan, C. Biris, N. Panoiu, M. Yu, D. Kwong, A. Stein, and C. Wong, "Zero phase delay in negative-refractive-index photonic crystal superlattices," *Nat. Photon.*, Vol. 5, 499–505, 2011.
40. Engheta, N., "Pursuing near-zero response," *Science*, Vol. 340, 286–287, 2013.
41. Lu, L., H. Gao, and Z. Wang, "Topological one-way fiber of second Chern number," *Nat. Commun.*, Vol. 9, 5384, 2018.
42. Zhou, M., L. Ying, L. Lu, L. Shi, J. Zi, and Z. Yu, "Electromagnetic scattering laws in Weyl systems," *Nat. Commun.*, Vol. 8, 1388, 2017.
43. Wang, C., H. Wang, L. Shen, R. Abdi-Ghaleh, M. Y. Musa, Z. Xu, and B. Zheng, "Structure-induced hyperbolic dispersion in waveguides," *IEEE Trans. Antennas & Propagation*, Vol. 67, 5463–5468, 2019.
44. Liberal, I., A. M. Mahmoud, Y. Li, B. Edwards, and N. Engheta, "Photonic doping of epsilon-near-zero media," *Science*, Vol. 355, 1058–1062, 2017.
45. Zhang, Y., Y. Luo, J. B. Pendry, and B. Zhang, "Transformation-invariant metamaterials," *Phys. Rev. Lett.*, Vol. 123, 067701, 2019.
46. Liu, R., Q. Cheng, T. Hand, J. J. Mock, T. J. Cui, S. A. Cummer, and D. R. Smith, "Experimental demonstration of electromagnetic tunneling through an epsilon-near-zero metamaterial at microwave frequencies," *Phys. Rev. Lett.*, Vol. 100, 023903, 2008.
47. Moitra, P., Y. Yang, Z. Anderson, I. I. Kravchenko, D. P. Briggs, and J. Valentine, "Realization of an all-dielectric zero-index optical metamaterial," *Nat. Photon.*, Vol. 7, 791–795, 2013.
48. Li, Y., S. Kita, P. Muñoz, O. Reshef, D. I. Vulis, M. Yin, M. Lončar, and E. Mazur, "On-chip zero-index metamaterials," *Nat. Photon.*, Vol. 9, 738–742, 2015.
49. Chu, H., Q. Li, B. Liu, J. Luo, S. Sun, Z. Hang, L. Zhou, and Y. Lai, "A hybrid invisibility cloak based on integration of transparent metasurfaces and zero-index materials," *Light Sci. Appl.*, Vol. 7, 50, 2018.
50. Caldwell, J. D., A. V. Kretinin, Y. Chen, V. Giannini, M. M. Fogler, Y. Francescato, C. T. Ellis, J. G. Tischler, C. R. Woods, A. J. Giles, M. Hong, K. Watanabe, T. Taniguchi, S. A. Maier, and K. S. Novoselov, "Sub-diffractional volume-confined polaritons in the natural hyperbolic material hexagonal boron nitride," *Nat. Commun.*, Vol. 5, 5221, 2014.
51. Woessner, A., M. B. Lundeberg, Y. Gao, A. Principi, P. Alonso-Gonzalez, M. Carrega, K. Watanabe, T. Taniguchi, G. Vignale, M. Polini, J. Hone, R. Hillenbrand, and F. H. L. Koppens, "Highly confined low-loss plasmons in graphene-boron nitride heterostructures," *Nat. Mater.*, Vol. 14, 421–425, 2015.
52. Ordal, M. A., R. J. Bell, R. W. Alexander, Jr., L. L. Long, and M. R. Querry, "Optical properties of fourteen metals in the infrared and far infrared: Al, Co, Cu, Au, Fe, Pb, Mo, Ni, Pd, Pt, Ag, Ti, V, and W," *Appl. Optics*, Vol. 24, 4493–4499, 1985.

Supporting Information for

"Superscattering of light in refractive-index near-zero environments"

Chan Wang, Chao Qian, Hao Hu, Lian Shen, Zuojia Wang, Huaping Wang, Zhiwei Xu, Baile Zhang, Hongsheng Chen, Xiao Lin

Supporting Information Guide:

Section S1. The influence of loss on the superscattering

This section discusses the influence of loss on the superscattering, and it serves as the complementary information for Figures 2 and 4.

The influence of BN's loss on the superscattering in Figure 2

The hexagonal boron nitride (BN) has two reststrahlen bands, namely 22.3-24.5 THz for the first reststrahlen band and 41.1-48.2 THz for the second reststrahlen band. In this work, the experimental data for the relative permittivity of BN is adopted[47, 48, S1, S2]. In short, BN's relative permittivity can be modelled by

$$\varepsilon_l = \varepsilon_l(\infty) + s_{v,l}\frac{\omega_{v,l}^2}{\omega_{v,l}^2 - i\gamma_{v,l}\omega - \omega^2}, l = \perp, \parallel \quad \text{(S1)}$$

where the subscripts $\perp$ and $\parallel$ refer to the component of permittivity perpendicular and parallel to the plane of each BN layer, respectively. Here we set the plane of each BN layer parallel to

the interface in Figures 2 and 3. For the in-plane permittivity, $\varepsilon_l(\infty)$=4.87, the real-valued constant $s_{v,l}$=1.83 (dimensionless coupling factor), the normal frequency of vibration $\hbar\omega_{v,l}$=170.1 meV, and the amplitude decay rate $\hbar\gamma_{v,l}$=0.87 meV. For the out-of-plane permittivity, $\varepsilon_l(\infty)$=2.95, $s_{v,l}$=0.61, $\hbar\omega_{v,l}$=92.5 meV, $\hbar\gamma_{v,l}$=0.25 meV.

For conceptual clarity, the imaginary part of BN's permittivity in Figure 2 is artificially neglected. As the complementary information for Figure 2, we consider the realistic complex value of BN's permittivity in Figure S1. In addition to the value of BN's permittivity, the other setup in Figure S1 are the same as Figure 2. While the BN's loss would decrease the total cross section at the frequency of superscattering, the phenomenon of superscattering can survive under the consideration of realistic BN's loss.

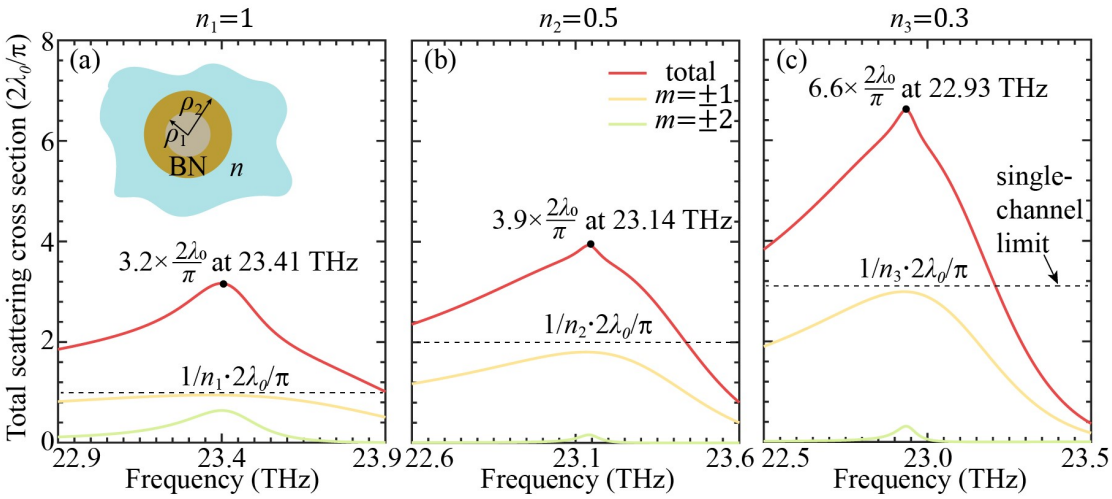

Figure S1. Influence of BN's loss on the superscattering in low-index environments. The realistic complex value of BN's permittivity from experiments[50,51,S1,S2] is considered here. In addition to BN's permittivity, the other setup in (a), (b) and (c) are the same as that in Figure 2(a), (b), and (c), respectively. The phenomenon of superscattering still exists under the consideration of BN's loss.

The influence of metal's loss on the superscattering in Figure 4

For metals, we model their relative permittivity by the Drude model, namely $\varepsilon_{\mathrm{m}} = 1 - \omega_p^2/(\omega^2 + i\gamma_d\omega)$. We adopt copper in the design of metal-based superscatterer in Figure4. Based on some experimental data[49, S3, S4], copper's plasma frequency is $\omega_p/2\pi = 1.8 \times 10^3$ THz, and its decay rate is $\gamma_d = 0.0012\omega_p$. For conceptual clarity in Figure 4, the value of γ_d is artificially set to be zero. As the complementary information for Figure 4, the value of $\gamma_d = 0.0012\omega_p$ is applied in Figure S2. In addition to the value of metal's permittivity, the other setup in Figure S2 are the same as Figure 4. Figure S2 shows that the superscattering can survive under the consideration of realistic metal's loss.

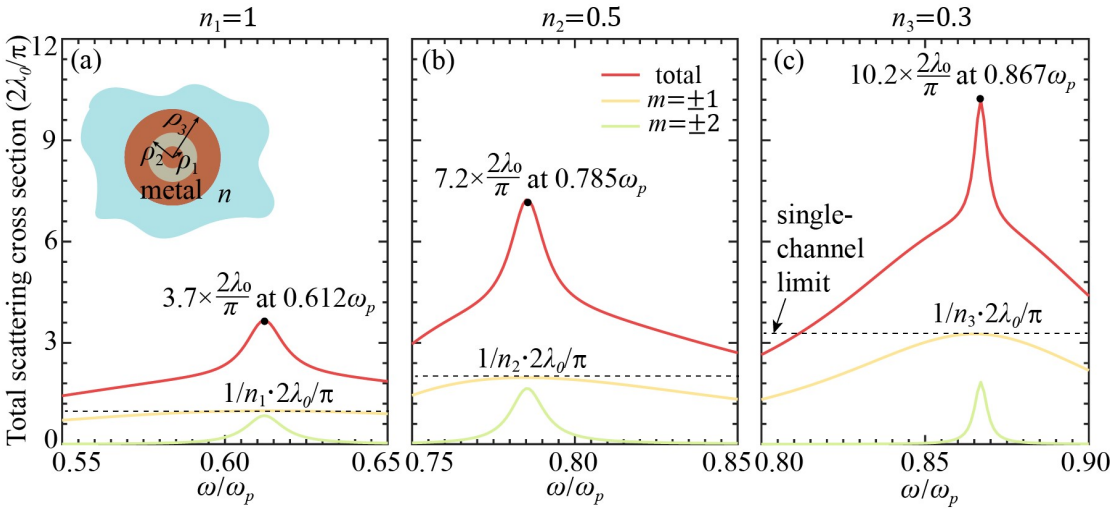

Figure S2. Influence of metal's loss on the superscattering in low-index environments. The realistic complex value of metal's permittivity from experiments[49, S3, S4] is considered here. In addition to metal's permittivity, the other setup in (a), (b) and (c) are the same as that in Figure 4(a), (b), and (c), respectively. The superscattering still exists in the presence of metal's loss.

Section S2. More examples of superscattering in low-index environments

As the complementary information for Figures 2 and 4, Figures S3 and S4 show the superscattering from subwavelength structures in the environment with $n = 0.1$. By maximizing the scattering contribution from channels with $m = \pm 1$ and $m = \pm 2$, Figures S3-S4 show that the total scattering cross section of the designed superscatterers at the frequency of superscattering can reach $40 \times 2\lambda_0/\pi$ in the environment with $n = 0.1$. In addition, the phenomenon of superscattering in Figures S3 and S4 is more sensitive to the working frequency than those in Figures 2 and 4.

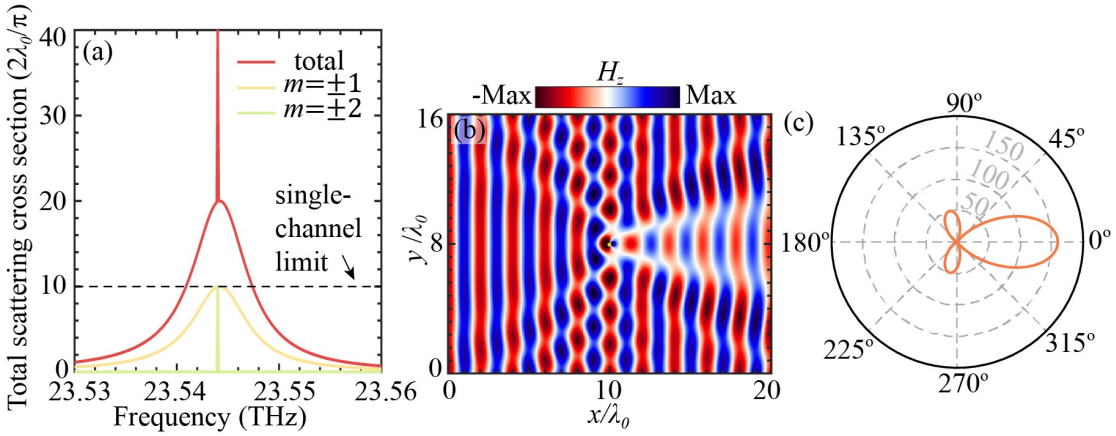

Figure S3. Superscattering in the environment with $n = 0.1$ induced by the degenerate resonance of BN's phonon polaritons. After the structural optimization, we have $\rho_1 = 1.80$ μm, $\rho_2 = 2.84$ μm, and $\varepsilon_d = 4.38$ for the scatterer. (a) Total cross section. (b) Distribution of magnetic field H_z around the scatterer at 23.544 THz. (c) Scattering cross section per azimuthal angle in the far field at 23.544 THz.

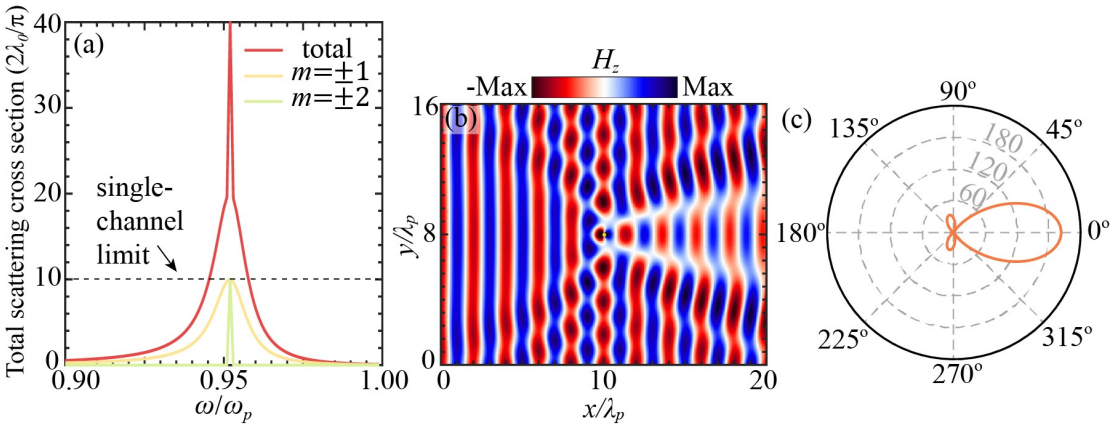

Figure S4. Superscattering in the environment with $n = 0.1$ induced by the degenerate resonance of metal plasmons. After the structural optimization, we have $\rho_1 = 0.035\lambda_p$, $\rho_2 = 0.182\lambda_p$, $\rho_3 = 0.453\lambda_p$, and $\varepsilon_d = 2.9$ for the scatterer. (a) Total cross section. (b) Distribution of magnetic field H_z around the scatterer at $0.952\omega_p$. (c) Scattering cross section per azimuthal angle in the far field at $0.952\omega_p$.

Besides, Figure S5(a) shows that the superscattering phenomenon always exists even if the low-index environment has a reasonable variation of refractive index. To be specific, the variation of refractive index (which is equivalent to the consideration of frequency dispersion) in the low-index environment mainly slightly shift the working frequency of superscattering. Moreover, since the superscattering phenomenon is induced by degenerate resonances, the superscattering phenomenon happens in a very narrow frequency range; see for example in Figure S5(a). Since we are interested in the frequency having the superscattering phenomenon, the frequency dispersion of the environment within the interested narrow frequency range is generally negligible. In addition, the requirement of $\varepsilon_r = \mu_r$ for the environment is not a strictly necessary condition for the realization of superscattering in low-index environment. For example, we also show in Figure S5(b) the superscattering phenomenon in low-index

environments with $\mu_r = 1$ and $\varepsilon_r < 1$.

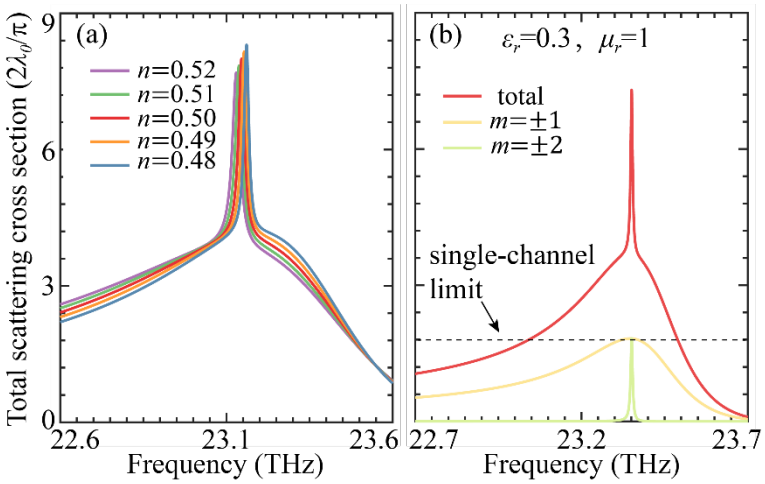

Figure S5. (a) Influence of environment's refractive index variation on the superscattering phenomenon. The basic structural setup is the same as that in Fig. 2(b), except for the refractive index of environment. Here $\varepsilon_r = \mu_r$. (b) Superscattering in low-index environments with $\varepsilon_r \neq \mu_r$. To be specific, here we set $\mu_r = 1$ and $\varepsilon_r = 0.3$. The basic structural setup is similar to that in Fig. 2(b) by setting $\rho_1 = 1.58$ μm, $\rho_2 = 2.72$ μm, and $\varepsilon_d = 4.29$.

Section S3. More information for the superscattering in Figure 4

Figure 4 shows the superscattering in low-index environments induced by the degenerate resonance of metal plasmons. Figure S6 provides another way to understand the influence of environments on the superscattering in Figure 4, by correspondingly showing the field distribution [Figure S6(a-c)] and the scattering cross section per azimuthal angle [Figure S6(d-f)].

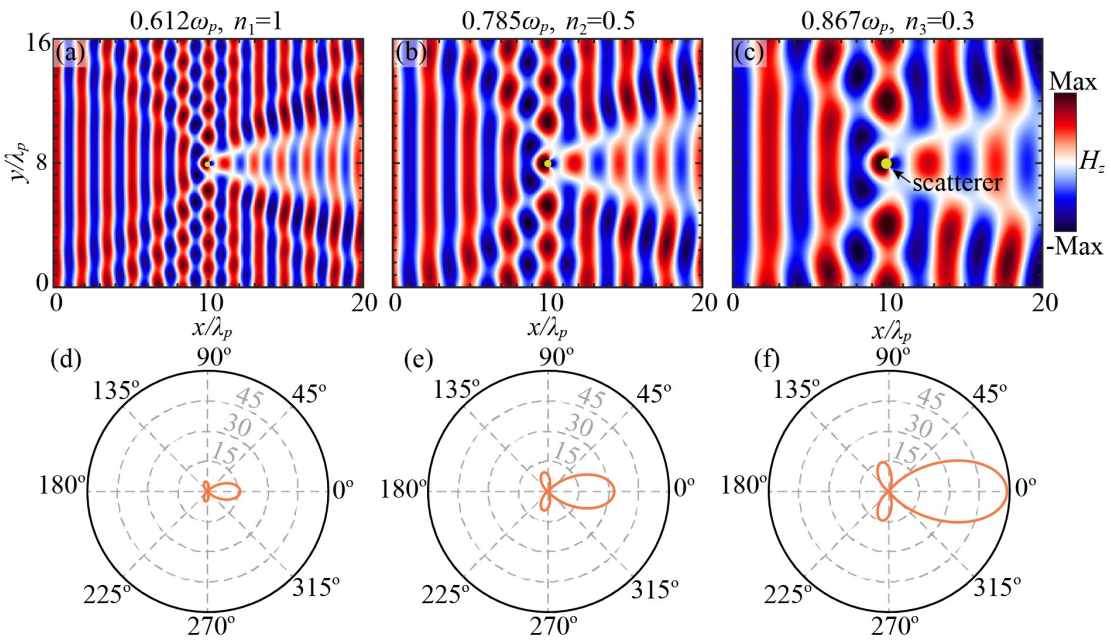

Figure S6. Near-field and far-field demonstration of superscattering in low-index environments induced by the degenerate resonance of metal plasmons. (a-c) Distributions of magnetic field H_z around the scatterer and (d-f) scattering cross sections per azimuthal angle in the far field at (a, d) $0.612\omega_p$, (b, e) $0.785\omega_p$ and (c, f) $0.867\omega_p$. These three frequencies correspond to the peak frequencies of the total cross section in Figure 4(a-c), respectively. The structural setups in (a, d), (b, e) and (c, f) are the same as those in Figure 4(a), (b), and (c), respectively. The incident TM waves propagate from left to right in (a-c).

Section S4. Superscattering in low-index environments by maximizing the contribution from more channels

As the complementary information for Figures 2 and 4, we provide the examples of superscattering in low-index environments by maximizing the scattering contribution from more channels, such as $1 \leq |m| \leq 3$ and $n = 0.5$ in Figures S7 and S8. Then Figures S7 and S8 show that the total cross section for the designed subwavelength scatters can reach $12 \times 2\lambda_0/\pi$ at the frequency of superscattering.

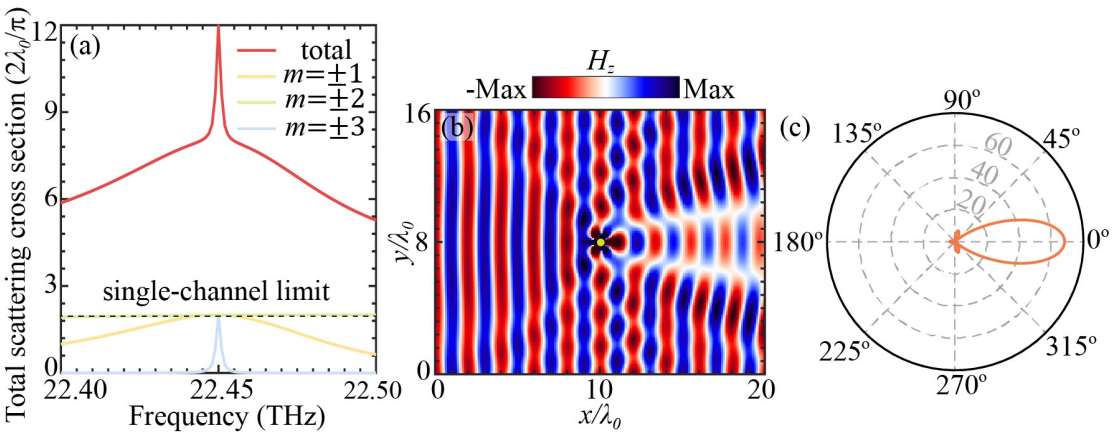

Figure S7. Enhanced superscattering in low-index environments induced by the degenerate resonance of BN's phonon polaritons. This figure serves as the complementary information for Figure 2. The basic structural setup here is similar to that in Figure 2, and we set $n = 0.5$. During the structural optimization, we maximize the scattering contribution from channels with $m = \pm 1$, $m = \pm 2$, and $m = \pm 3$. After the structural optimization, we have $\rho_1 = 0.74\ \mu m$, $\rho_2 = 5.12\ \mu m$, and $\varepsilon_d = 1.33$ for the scatterer. (a) Total cross section. (b) Distribution of magnetic field H_z around the scatterer at 22.45 THz. (c) Scattering cross section per azimuthal angle in the far field at 22.45 THz.

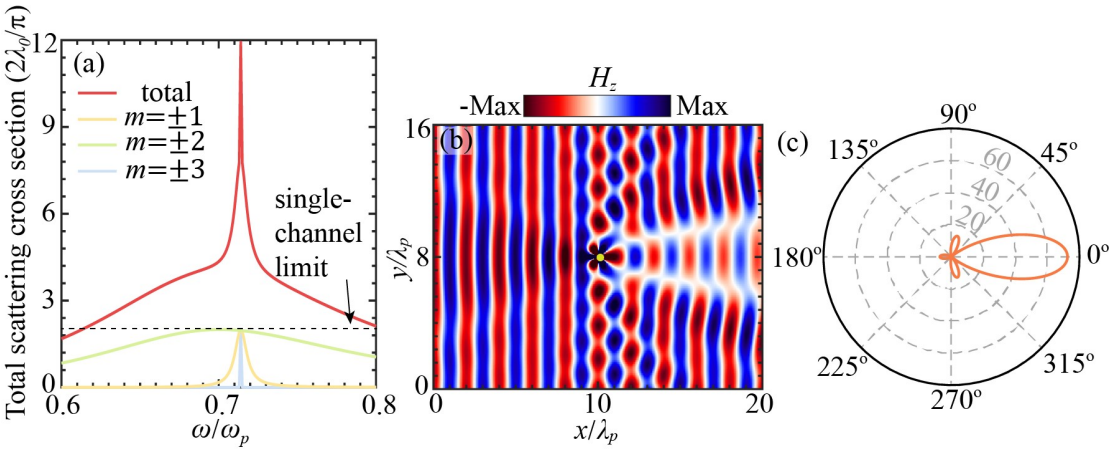

Figure S8. Enhanced superscattering in low-index environments induced by the degenerate resonance of metal plasmons. This figure serves as the complementary information for Figure 4. The basic structural setup here is similar to that in Figure 4, and we set $n = 0.5$. During the

structural optimization, we maximize the scattering contribution from channels with $m = \pm 1$, $m = \pm 2$, and $m = \pm 3$. After the structural optimization, we have $\rho_1 = 0.272\lambda_p$, $\rho_2 = 0.287\lambda_p$, $\rho_3 = 0.304\lambda_p$, and $\varepsilon_d = 3.4$ for the scatterer. (a) Total cross section. (b) Distribution of magnetic field H_z around the scatterer at $0.714\omega_p$. (c) Scattering cross section per azimuthal angle in the far field at $0.714\omega_p$.

References:

[S1] S. Dai, Q. Ma, T. Andersen, A. Mcleod, Z. Fei, MLiu, M. Wagner, K. Watanabe, T. Taniguchi, M. Thiemens, *Nat. Commun.* **2015**, *6*, 6963.

[S2] E. Yoxall, M. Schnell, A. Y. Nikitin, O. Txoperena, A. Woessner, M. B. Lundeberg, F. Casanova, L. E. Hueso, F. H. Koppens, R. J. Hillenbrand, *Nat. Photon.* **2015**, *9*, 10.

[S3] L. Schulz, *JOSA* **1954**, *44*, 7.

[S4] L. Schulz, *Adv. Phys.* **1957**, *6*, 21.